Oxygen-Regulated Spontaneous Solid Electrolyte Interphase Enabling Ultra-Stable Solid-State Na Metal Batteries

Keshuang Cao [a, b, 1], Yufan Xia [a, b, 1], Haosheng Li [a, b], Huiqin Huang [a, b], Sikandar Iqbal [b], Muhammad Yousaf [b], Ben Bin Xu [c], Wenping Sun [a], Mi Yan [a], Hongge Pan [d], Yinzhu Jiang[a, b*]

[a] School of Materials Science and Engineering, State Key Laboratory of Clean Energy Utilization, Zhejiang University, Hangzhou 310027, China

[b] ZJU-Hangzhou Global Scientific and Technological Innovation Centre, Zhejiang University, Hangzhou 311200, China

[c] Mechanical and Construction Engineering, Faculty of Engineering and Environment, Northumbria University, Newcastle upon Tyne NE1 8ST, UK

[d] Institute of Science and Technology for New Energy, Xi'an Technological University, Xi'an 710021, China

[1] These authors contributed equally to this work.

[*]Corresponding author. E-mail address: yzjiang@zju.edu.cn (Y. Jiang)

Abstract

Solid-state sodium metal batteries utilizing inorganic solid electrolytes (SEs) hold immense potentials such as intrinsical safety, high energy density, and environmental sustainability. However, the interfacial inhomogeneity/instability at the anode-SE interface usually triggers the penetration of sodium dendrites into the electrolyte, leading to short circuit and battery failure. Herein, confronting with the original nonuniform and high-resistance solid electrolyte interphase (SEI) at the Na-$Na_3Zr_2Si_2PO_{12}$ interface, an oxygen-regulated SEI innovative approach is proposed to enhance the cycling stability of anode-SEs interface, through a spontaneous reaction between the metallic sodium (containing trace amounts of oxygen) and the $Na_3Zr_2Si_2PO_{12}$ SE. The oxygen-regulated spontaneous SEI is thin, uniform, and kinetically stable to facilitate homogenous interfacial Na^+ transportation. Benefitting from the optimized SEI, the assembled symmetric cell exhibits an ultra-stable sodium plating/stripping cycle for over 6600 h under a practical capacity of 3 mAh cm^{-2}. Quasi-solid-state batteries with $Na_3V_2(PO_4)_3$ cathode deliver excellent cyclability over 500 cycles at a rate of 0.5 C with a high capacity retention of 95.4%. This oxygen-regulated SEI strategy may offer a potential avenue for the future development of high-energy-density solid-state metal batteries.

Keywords: Na metal anode; Solid-state batteries; NaSICON; Anode interface; Solid electrolyte interphase

1. Introduction

Solid-state sodium metal batteries incorporating solid electrolytes (SEs) are widely regarded as a prime contender for next-generation energy storage systems with the merits of good safety, resource sustainability, and high energy density [1-3]. Among numerous Na-conducting SEs, $Na_3Zr_2Si_2PO_{12}$ (NZSP) with Na super ionic conductor (NaSICON) structure is one of the top picks, for its high ionic conductivity, wide electrochemical window, and convenient access via conventional synthesis methods [4]. Such ceramic SEs were initially anticipated to inhibit dendrite penetration under their inherent mechanical strength and high ionic transference number [5-7]. Unfortunately, they suffer from serious dendrite growth under practical test conditions, leading to the explicit deterioration in performance and even the short-circuit, which severely hampers their practical implementation [8]. Therefore, the interfacial inhomogeneity and/or instability between anode and SEs are widely recognized as the primary causes of localized preferential electrodeposition and subsequent dendrite growth [9, 10].

The utilization of anode-SE interlayers stands as the predominant approach to mitigate the interfacial challenges [11-16]. Such interlayer takes advantage of the replacement/alloying reaction of highly active metal anode with the buffer layer, to improve interfacial compatibility with the Na anode and homogenize Na^+ transport kinetics to inhibit dendrite growth. However, the effectiveness of functional interlayers will further deteriorate when cycling at high capacity/current density upon repeated Na plating and stripping, thereby severely degrading the validity for practical applications. More problematically, the presence of conductive components within the interlayer may advertently trigger the deposition of metal between the interlayer and SE, inducing its complete failure [9]. In this view, constructing an intrinsically stable interface between the metallic anode and SE is a prerequisite for developing solid state metal batteries.

According to frontier molecular orbital theory [17], the inherent discrepancy of chemical potential between Na metal and NZSP engenders spontaneous chemical reactions that form solid electrolyte interphase (SEI) [18]. Drawing upon the extensive exercises in stabilizing Li/Na metal anodes in liquid electrolytes [19-21], the deliberate

harnessing of spontaneous reactions between Li/Na metal and precisely tailored liquid electrolytes has demonstrated remarkable efficacy in optimizing SEI [22-24]. The optimized SEI is generally self-limiting and can promote the uniformity of Li/Na plating/stripping reaction in nano- and macro-scales, thus greatly inhibiting the dendrite growth. It inspires, that a similar principle can be applied to solid-state batteries. Under this guidance, Martin's group [25, 26] has reported a stable oxysulfide glass SE ($Na_3PS_{4-x}O_x$, $0 < x \leq 0.6$), which reacts with sodium metal to form a self-passivating SEI that can significantly reduce the unfavorable reactions of sulfide electrolytes and Na metal. By modulating the composition of β"-Al_2O_3, Wang and co-workers [27] developed a thin and robust β-$NaAlO_2$-rich SEI layer at the interface with Na metal to replace the original thick and electron-conductive SEI layer, thus greatly inhibiting the penetration of Na dendrites. However, solutions to optimize the original SEI have rarely been reported in NZSP-based solid-state batteries, which is expected to break the bottleneck of premature short-circuiting caused by inhomogeneous/unstable Na-NZSP interface.

Herein, the interface chemistry between Na and NZSP is first comprehensively investigated, revealing that the original SEI at the Na-NZSP interface is heterogeneous with large interface resistance, which poses a significant risk of dendrite penetration upon cycling. In combination with first-principle calculations, it has been found that the interstitial oxygen defect atom can attract electrons around the sodium atom, and the surface work function value can be further increased after adsorption and embedding oxygen molecules on the Na (110) surface, implying that the introduction of oxygen molecules can reduce the chemical activity of sodium metal. Therefore, a novel method of introducing oxygen into Na metal by thermal annealing is implemented for the first time to reduce its chemical activity and to yield a thin and homogeneous SEI to host a uniform plating/stripping process of Na. The oxygen-regulated spontaneous SEI is kinetically stable and has no additional interface resistance. Furthermore, it is also found that the homogeneous SEI between oxygen-rich Na and NZSP provides more uniform ion transport to inhibit the formation of interface voids, thus greatly improving the interfacial stability. Benefiting from the

favorable anode-SE interface, the symmetric cell remains stable for 6600 h under 0.5 mA cm^{-2}, 3 mAh cm^{-2}, and the full cell exhibits excellent cycle performance over 500 cycles at 0.5 C (1 C = 117 mA cm^{-2}) without significant capacity degradation.

2. Experimental

2.1 Materials synthesis

The $Na_3Zr_2Si_2PO_{12}$ solid-state electrolyte was synthesized through a solid-state reaction method. Briefly, the stoichiometric raw materials of Na_2CO_3 (≥ 99.99%, Aladdin), ZrO_2 (≥ 99.99%, Aladdin), SiO_2 (≥ 99.99%, Aladdin), and $NH_4H_2PO_4$ (≥ 99%, Aladdin) were mixed for 12 h by ball-milling with a proper amount of ethanol solvent. The 15% excess Na_2CO_3 and $NH_4H_2PO_4$ were added to compensate for the loss of Na and P at high temperatures and decrease the impurity content. The raw mixture was pre-sintered at 1000 °C for 8 h under an air environment. After ball milling for 12 h, the obtained white powder was pressed into pellets at a pressure of 300 MPa. Finally, the NZSP pellet was obtained after being sintered at 1240 °C for 6 h under an air environment. After sintering, the obtained pellets were immediately transferred to a glove box filled with argon for storage, to prevent reaction with air and moisture.

Preparation of oxygen-rich Na (ORNa) was conducted in an argon-filled glove box ($O_2 \leq 0.1$ ppm, $H_2O \leq 0.1$ ppm). After sodium metal (≥ 99.7%, Sinopharm) was taken out of kerosene and wiped clean, the surface oxide layer was removed with a scalpel to obtain fresh sodium metal. 2 g of fresh Na metal was heated to 350 °C in a nickel crucible and stirred continuously for 10 min to promote full contact with the atmosphere. Then, the metal was cooled down, pressed mechanically, and then punched into discs to be applied as the ORNa anodes. The pristine Na anode was obtained by stamping fresh sodium blocks.

2.2 Characterization

Time-of-flight secondary ion mass spectrometry (TOF-SIMS) data were recorded from TOF-SIMS5-100 (IONTOF) with Cs^+ as sputter species and Bi^+ as primary ions, and the analysis area was (100 × 100) μm^2. The same experimental parameters were

used for the transverse comparison of samples. X-ray photoelectron spectroscopy (XPS) characterization was conducted at room temperature on Thermo Scientific K-Alpha using monochromatic Al Kα, in which the samples were transferred to XPS equipment by a special transition chamber to prevent them from reacting with air. The morphologies were observed by field emission scanning electron microscopy (SEM, HITACHI SU-8010). The surface structure was detected by grazing incidence X-ray diffraction (GIXRD; Smartlab 9 kW, Rigaku Corporation; Cu Kα) measurements, and an incidence angle of 0.5° was used. Bruker D2 Phaser (CuKα radiation, λ = 1.5405 Å) X-ray diffraction analyzer was employed to record the X-ray diffraction (XRD) pattern.

2.3 Cell assembly and electrochemical measurements

The symmetric cells were assembled with CR2032 coin-type cells in an Ar-filled glove box to evaluate the stability of the anode-SE interface. For the assembly of pristine Na symmetric cells, the prepared fresh Na discs were placed on both sides of NZSP pellets with stainless steel as current collector, and then 0.08 tons of mechanical pressure was applied to eliminate the initial poor physical contact. A packaging machine (MSK-160E) was used to encapsulate all coin cells with a force of 0.4 tons. For the ORNa symmetric cells, the prepared ORNa discs were used as electrodes, and the rest was the same with pristine Na symmetric cells.

$Na_3V_2(PO_4)_3$ (NVP) was purchased from Hubei Ennaiji Company. The cathode slurry was prepared by mixing NVP, Super P and poly(vinylidene fluoride) (PVDF) with a weight ratio of 8:1:1 in *N*-methyl-2-pyrrolidone (NMP) solvent. The slurry was dried at 80 °C in vacuum overnight after casting on the carbon-coated Al foil. The mass loading of the active material NVP was 3−4 mg cm^{-2}. 5 μL liquid electrolyte of 1 mol L^{-1} $NaPF_6$ in EC/DEC/PC (4:4:2, v:v:v) with 5.0% FEC was adopted to wet the cathodic side.

The electrochemical impedance spectroscopy (EIS) of the battery under different charge states was measured by an electrochemical workstation (PARSTAT 4000A, Princeton Instruments) in a frequency range from 3 MHz to 0.1 Hz with an applied voltage of 5 mV. Distribution of relaxation time (DRT) analyses were conducted by a MATLAB GUI toolbox named DRTtools, which was developed by Ciucci's group [28].

Tikhonov regularization was utilized to fit discrete experimental data in a nonlinear least square manner, and Gaussian method was used to discretize data. Galvanostatic cycling experiments were performed on a NEWARE BTS-5 battery-test system.

2.4 Computational method

The first-principle calculations were performed using the Vienna *Ab initio* Simulation Package (VASP) (version 6.3.0) [29, 30] with the projector augmented-wave (PAW) method [31] and the Perdew-Burke-Ernzerhof (PBE) [32] exchange-correlation functional. The energy cutoff for the plane-wave basis was set to 500 eV to ensure the convergence of the calculations. We considered the bulk Na metal (3×3 supercell) as well as the stable Na metal surface: Na (110) [33, 34]. The Brillouin zone integration was performed using the Γ-centered mesh with k-point of 2×2×1 and 3×3×3 for the surface and bulk calculations, respectively. Na (110) surface was constructed with a vacuum region of 15 Å between the periodic images to avoid any interactions between neighboring cells. The bottom two layers of the Na (110) surface were constrained to simulate the bulk properties of the system. The structure optimization and self-consistent field (SCF) calculations were performed until the energy and forces were converged to within 10^{-5} eV and 0.02 eV $Å^{-1}$, respectively. We applied the D3 correction [35] to account for the van der Waals interactions between the atoms for surface calculations. The data post-processing was used by VASPKIT code [36] and the crystal structures were visualized using VESTA [37].

3. Results and discussion

3.1 The interface of pristine Na and NZSP

All-solid-state symmetric cells were assembled using pure Na metal as the electrode and NZSP as the SEs to investigate the formation of the original SEI in Na-NZSP interface and its influence. The XRD patterns and ionic conductivity test of as-synthesized NZSP pellet are shown in Fig. S1 (online), which suggests that the NZSP pellet has a high purity and ionic conductivity. To eliminate the initial poor physical contact, the sintered NZSP pellets were immediately transferred to the glove box for

storage (preventing the surface from reacting with air and moisture), and mechanical pressure was used to attach the Na metal to the NZSP pellet. As such, the initial interface resistance of Na and NZSP in newly assembled Na symmetric cells optimized to almost 0 Ω cm^{-2} (Fig. 1a), which indicates that the initial interface contact is intimate. However, it is observed that the interface resistance of Na/NZSP/Na symmetric cell under zero bias steadily increases continuously within a few days, indicating continuous interfacial reactions at the interface. Thereafter, the interface resistance is stabilized around 170 Ω cm^{-2} (Fig. 1b), suggesting that the original SEI formed after the sufficient interfacial reaction is kinetically stable, consistent with previous studies [38, 39]. However, the large interface resistance indicates the sluggish sodium ion diffusion kinetics within the interfacial layer.

We further assessed the effect of original SEI on interfacial stability by cycling tests of symmetric cells (Fig. 1c). Due to the joint contribution from interface reaction and interface contact loss, the overpotential of fresh symmetric cells increases continuously during cycling, and a short circuit occurs at around 140 h. To avoid the interference of interface reaction on the overpotential, an aged symmetric cell with a stable interface (standing for more than 30 d) was used for testing. An obvious increase of overpotential can still be observed in the aged symmetric cell during the first cycle, then a quick short circuit occurs in the second cycle. Considering that the interface reaction has been stabilized, the overpotential increase can be attributed to the contribution of interface contact deterioration. Therefore, the inferior electrochemical performance of aged batteries suggests that the formation of SEI between Na and NZSP has a detrimental effect on the stability of their interface.

Subsequently, TOF-SIMS was utilized to analyze the interfacial chemistry of the Na-NZSP interface. In Fig. 1d, the 3D mapping images of secondary-ion fragments of interest, reveal very high intensity of Cs_2P^+ and $CsNaO^+$ in some regions but relatively low intensities of host elements Zr^+ and Si^+, indicating that the signals of Cs_2P^+ and $CsNaO^+$ are related to the interface reaction products. The reaction products distribute perpendicular to the interface layer, with significant variation in penetrating depth. The occurrence of nonuniform interfacial reactions is responsible for the resulting

inhomogeneous interfacial layer and large interface resistance. Hence, the degradation mechanism of the Na-NZSP interface can be illustrated in Fig. 1e: the uneven spontaneous interface reaction layer leads to uneven interface ion transport in the stripping process to create the interface voids, which leads to the current contraction in the subsequent sodium deposition, and eventually results into the dendrite penetration in NZSP.

3.2 Construction of oxygen-rich Na

The high reactivity of Na metal and the high electronic conductivity of reaction products with NZSP may be the origin of undesirable SEI. Inspired by available studies and considering the key role oxygen may play in stabilizing the interfacial reactions of alkali metal anodes [25-27, 40, 41], the effect of oxygen introduction on sodium metal was calculated using the first-principle calculations. Fig. 2a presents the charge density difference of bulk sodium metal crystal structure with an interstitial oxygen defect. Obvious overlapped electron cloud density between Na and O atoms is found, indicating the stable combining ability and electron transfer from Na atoms to near O atom. Specifically, the high electronegativity of oxygen element influences the charge distribution of Na atoms, which further reduces its reactive activity. Similar charge transfer has been demonstrated in the Na metal surface (Fig. S2 online). The change in work function of the Na (110) surface before and after the adsorption of O_2 was calculated with the corresponding optimized adsorption structures are shown in Fig. S2 (online). The oxygen molecules are well adsorbed and embedded on the Na (110) surface due to the relatively large distance between Na atoms. The calculated results of the work function are shown in Fig. 2b, indicating that the work function of the Na (110) + O_2 surface is larger, from 2.83 eV on the original Na (110) surface to 2.88 eV (average value), confirming reduced reactivity of surface electrons after the introduction of oxygen [42]. The above theoretical calculations collectively demonstrate the feasibility of introducing oxygen into sodium metal to reduce its chemical reactivity.

Even though the oxygen content in argon-filled glove boxes is usually at a very low level ($\leq$ 0.1 ppm), the existence of oxygen cannot be ignored, especially for highly reactive substances such as alkali metals [43], e.g., fresh sodium metals gradually lose

their metallic luster and undergo prominent surface oxidation after a period of time in the glove box. Considering that oxygen has a certain solubility in sodium metal [44-46], we heat the sodium metal in a glove box and constantly stir it to dissolve the trace amounts of oxygen in the glove box atmosphere into the liquid sodium metal. The as-obtained oxygen-rich Na metal is cooled and applied as the metal anode, denoted as ORNa. TOF-SIMS depth profiling with ultrahigh elemental sensitivity is conducted to qualitatively study the elemental composition of Na metal. Although the samples were transferred by a special high vacuum tube, the surface oxidation of Na is inevitable due to its high activity. TOF-SIMS results (Fig. 2c, d) show that the surface oxidation layer of ORNa is removed after sputtering for 700 s. While the pristine Na takes 2800 s to be removed under the same condition, highlighting the significantly reduced surface oxidation of ORNa and its relatively lower chemical activity. More importantly, the O/Na ratio in the bulk of pristine Na is 0.32, while that in the ORNa is 0.61. Considering that the main element in both Na and ORNa is sodium, this indicates that the oxygen content in ORNa is higher, confirming the successful introduction of oxygen into ORNa. The XPS test is performed after etching the surface oxide layer produced during the sample transfer process (Fig. 2e, f and Fig. S3 online). It is found that the binding energy of Na^0 in the ORNa is higher (+0.4 eV), probably due to the effect of O atoms on sodium chemical environment. The electron paramagnetic resonance (EPR) test (Fig. S4 online) unveils a wide peak of ORNa with an increased asymmetry degree, reflecting the difference in the environment surrounding the electrons in ORNa and Na due to the introduction of oxygen. Moreover, the Na^+/ORNa couple exhibited a higher redox potential of 0.5 mV compared to the Na^+/Na couple (Fig. S5 online), corresponding to the increased work function [42], consistent with first-principle calculation results. In conclusion, the above characterization demonstrates the successful introduction of oxygen in ORNa.

3.3 Interface chemistry between ORNa and NZSP

The interface chemistry between ORNa and NZSP was investigated to examine the effect of introducing oxygen into Na on interfacial reaction. SEM images (Fig. 3a, b) show the obscured NZSP grain boundaries and some small particles on the NZSP

crystal surface after contacting with sodium metal. In contrast, the surface of NZSP after contact with ORNa presents a subtle change, and the original grains can be identified (Fig. 3c). In the TOF-SIMS depth profile curves (Fig. S6 online), the signal intensities of Na, P and O gradually decrease with the deepening of etching depth and then tend to be stable, while the signal intensities of Zr and Si basically remain unchanged, indicating a Na_xPO_y-dominant interphase forms on both Na-NZSP and ORNa-NZSP interface. TOF-SIMS high-resolution imaging results are shown in Fig. 3d; the intensity distribution of secondary-ion fragments of Zr^+, Si^+, Cs_2P^+, Cs_2O^+, and $CsNaO^+$ are heterogeneous across the surface of NZSP after contact with pristine Na, indicating a spatial, preferential reaction of Na with the NZSP. However, after contact with ORNa, the secondary ion fragments appear to be very uniform on the NZSP surface (Fig. 3e), and in 3D TOF-SIMS images (Fig. 3f), the Cs_2P^+ and $CsNaO^+$ fragments are concentrated on the surface, demonstrating the presence of a thinner and uniform SEI layer at the ORNa-NZSP interface.

XPS characterization was employed to study the chemical states of composing elements for SEI in Na-NZSP and ORNa-NZSP. The binding energies of Na (Fig. 3g) and Zr (Fig. 3h) on both Na-NZSP and ORNa-NZSP surfaces show a shift to lower energy, indicating that the SEI layer is composed of a partially reduced NZSP surface.[47] Additional shoulder peaks appear at low binding energies (E_B (Zr $3d_{5/2}$) = 180.9 eV) in the spectra of Zr 3d for Na-NZSP, indicating a chemical valence between Zr^{2+} and Zr^{3+} [48], while there is no obvious change for ORNa-NZSP. The reduced zirconium species is probably from ZrSi, which is one of the possible products after NZSP contacts with Na metal [38]. The formation of conductive ZrSi is unfavorable as it leads to continuous interfacial reactions, which may be the main reason for the thicker reaction layer observed in Na-NZSP. The chemical state of Si^{2-} from ZrSi is absent in Si 2p (Fig. S7a online), probably due to its reaction with the inevitable oxygen and moisture in the transfer, and then quickly oxidized again to Si^{x+} [38]. In XPS spectra of P 2p (Fig. 3i), a new doublet located at lower binding energy (E_B (P $2p_{3/2}$) = 132.7 eV) appears in both Na-NZSP and ORNa-NZSP, in good agreement with the TOF-SIMS results, which can be assigned to Na_xPO_y. The difference is that ORNa-NZSP has a lower content for

reduction products, indicating a lower reactivity of ORNa.

GIXRD was utilized to study the surface structure evolution of NZSP after the contact with Na and ORNa (Fig. S8 online). Compared with the pristine NZSP, the contacted NZSP shows a decreased peak intensity and a broadened diffraction peak compared with the pristine NZSP, showing a decrease in crystallinity. Interestingly, new peaks appear in ORNa-NZSP, which can be indexed to $Zr(PO_3)_4$ (PDF#73-0619). It proves that zirconium in NZSP exists on the surface in the form of $Zr(PO_3)_4$ after reacting with ORNa, and it cannot be distinguished in the Zr 3d spectrum, probably owing to its similarity in elemental valence to that in NZSP. The formation of electron-insulating $Zr(PO_3)_4$ may passivate ORNa to prevent the reaction from continuing [49], and thus the spontaneous SEI layer between ORNa and NZSP is thin.

Overall, the above investigations on interface chemistry reveal some important discoveries. In spatial distribution, the SEI of ORNa shows a significantly improved uniformity and a reduced thickness, which is beneficial to realize uniform electrochemical reactions. Regarding material composition, the reaction layer between Na or ORNa and NZSP is mainly composed of Na, P, and O elements, suggesting the formation of a dominant Na_xPO_y-interphase. The electronic conductive product ZrSi exists in the Na-NZSP reaction layer, which may cause a large thickness of SEI. However, as for the ORNa-NZSP interface, zirconium exists in the electronic insulating product $Zr(PO_3)_4$, which can passivate ORNa to prevent the interface reaction from continuing. Although the exact mechanism leading to this difference in reaction products remains unclear, it is speculated that the variation may be attributed to the introduction of oxygen or the reduced chemical activity in ORNa.

3.4 Stability of ORNa-NZSP interface

To evaluate the impact of optimized SEI on the interface stability, all-solid-state symmetric cells of ORNa are assembled and tested. Consistent with the fresh Na symmetric cell, the initial interface resistance of the fresh ORNa symmetric cell is 0 Ω cm^{-2}. The difference is that the impedance spectrum of the ORNa symmetric cell has no change during 5 months of standing, and the interface resistance remains negligible (Fig. 4a). This confirms that the interfacial reaction layer between ORNa and NZSP is

kinetically stable, and the thinner interfacial layer does not introduce additional interfacial resistance.

In the critical current density (CCD) test at 60 °C (Fig. 4b), ORNa exhibits an excellent high current tolerance, and the overpotential remains stable under a gradually increasing current density. In contrast, the Na symmetric cell shows rapid polarization aggravation from the current density of 0.8 mA cm^{-2} and a short circuit at 2.8 mA cm^{-2} (Fig. 4c). The overpotential is extremely large and unstable due to the sluggish interfacial Na^+ migration and interface contact loss. The average CCD of ORNa symmetric cell (Fig. 4d) is about 6.3 mA cm^{-2}, three times higher than that of pristine Na (2 mA cm^{-2}). In the long-term cycling tests at room temperature (RT, Fig. 4e), ORNa symmetric cell exhibits a small voltage hysteresis (~50 mV) and negligible voltage fluctuation at a current density of 0.5 mA cm^{-2} and a practical capacity of 3 mAh cm^{-2}. More importantly, it demonstrates remarkable long-term stability lasting for over 6600 h. To the best of our knowledge, this is the first time that solid-state Na metal symmetric cell based on NZSP has achieved such stable long-term cycling under practical conditions. In Fig. 4g, we compare the electrochemical performance of this work with various recently reported symmetric cells using NZSP as the solid electrolyte, and our ORNa symmetric cell shows superiority to other works, as listed in Table S1 (online). At 60 °C (Fig. 4f), the ORNa symmetric cell can stably cycle for over 6800 h under more stringent test conditions (2 mA cm^{-2}, 2 mAh cm^{-2}) without short circuit. The excellent electrochemical performance confirms the high cycling stability of the ORNa-NZSP interface, which comes from the uniform plating/stripping process promoted by the optimized SEI on ORNa.

To demonstrate the critical role of oxygen, a set of control experiments is designed, with the metal sodium heated without stirring. The continuous interfacial reaction can still be observed in the time-resolved impedance spectrum of assembled symmetrical battery (Fig. S9a online), and the corresponding CCD is a low value of (2.8 mA cm^{-2}, Fig. S9b online). It seems that the oxygen is blocked by the surface layer without stirring, therefore, it cannot fully engage with the sodium. As a result, no explicit improvement is shown in the sample without introducing oxygen. Moreover, to achieve

a controllable synthesis, it is found that the addition of trace sodium peroxide (Na_2O_2) as a source of oxygen to Na metal can fulfill the same purpose (Fig. S10 online), leading to improved interface stability between Na and NZSP and significantly improving performance.

3.5 Stability mechanism of ORNa-NZSP interface

Considering the exceptional performance of ORNa, besides the known interface chemistry between ORNa and NZSP, it is also essential to deeply investigate the transition of the interface evolution mechanism throughout the entire cycling process. In the voltage curves of the symmetric cells during cycling process (Fig. 5a), an increase in the overpotential of the Na symmetric cell can be observed. In contrast, the voltage of the ORNa symmetric cell remains almost constant. The interface resistance of the Na symmetric cell continues to increase during the discharge and charge processes (Fig. 5b), indicating that the continuous formation of interface voids. After undergoing a complete cycle, the interface resistance cannot be restored to the initial state, and this irreversibility causes poor cycle stability. On the contrary, the impedance spectrum of the ORNa symmetric cell remains constant throughout the discharge and charge processes with no additional interface resistance (Fig. 5c), suggesting the high uniformity and reversibility of the electrochemical reaction on a void-free interface.

As the formation of interface voids mainly occurs in the process of Na stripping, we next evaluate the evolution of interfacial electrochemical process during stripping by applying operando desodiation with EIS measurement and DRT analysis. During stripping (Fig. 5d), the overpotential of Na symmetric cell increases continuously during constant current polarization, manifesting large polarization, whereas the overpotential of the ORNa symmetric cell is in a relatively stable state within 20 h, indicating different electrochemical behaviors on the interface during galvanostatic polarization. Since the deposition of sodium usually does not lead to an increase in overpotential [50], the change in overpotential can be attributed to the stripping of Na under galvanostatic polarization.

During the above galvanostatic polarization process, EIS is measured at an interval of every 30 min. DRT analysis technology is applied to improve the accuracy of kinetic

interpretation in time scale and to identify the specific electrochemical processes in the anode-SE interface during galvanostatic polarization. The increased impedance of Na symmetric cell during polarization corresponds to about 10^{-3} -10^{-2} s (Fig. 5e), which may correspond to the charge transfer process of sodium metal with solid electrolyte [51]. Based on the available experimental results, it is supposed that the main failure mechanism of the Na-NZSP interface during galvanostatic stripping is due to the deterioration of the interfacial contact, as the continuous formation of interfacial voids reduces the effective reaction area and leads to an increase in interfacial charge transfer resistance. In contrast, the increase in additional resistance of the ORNa symmetric cell during galvanostatic polarization is minor (Fig. S11 online), suggesting a more stable interface. In addition, the corresponding relaxation time is 10^{-5} s (Fig. 5f), which is significantly different from Na symmetric cell. The high-frequency response in this region usually corresponds to the conduction-based process [51], it may come from the increased diffusion resistance in the ORNa-NZSP interface. Moreover, a richer O content on the surface of ORNa after sodium stripping can be observed in the XPS spectra (Fig. S12 online). And when 1 mAh cm^{-2} sodium is stripped, the voids can be observed at the interface of Na-NZSP (Fig. 5g and Fig. S13 online), while the interface of ORNa-NZSP remains as a close contact (Fig. 5h), suggesting the high uniformity of sodium stripping process. Therefore, we can infer that with the continuous stripping of Na, oxygen element is enriched on the ORNa surface, which increases the resistance of ion diffusion at the interface leading to an increase in interface resistance, rather than the gradual formation of numerous interfacial voids as in the case of pristine Na (the mechanism of void formation is shown schematically in Fig. 1e).

To conclude, the ORNa mechanism for enhancing interfacial cycling stability can be succinctly represented in Fig. 5i. Incorporating oxygen into ORNa leads to a modification of sodium atom's electronic environment, thereby decreasing Na metal chemical reactivity. As a result of a thin and highly homogenous SEI formed at the ORNa-NZSP interface through an *in-situ* reaction. This spontaneously formed, oxygen-regulated SEI impedes continuous Na-NZSP reactions without inducing additional resistance. Moreover, the optimized SEI promotes the uniform Na stripping/plating

process at the interface, effectively inhibiting the formation of interfacial voids and thus significantly enhancing the interfacial cycling stability of ORNa-NZSP.

3.6 Quasi-solid-state battery performance

We further assembled quasi-solid-state batteries using NZSP pellet as the electrolyte and NVP as the cathode, as a demonstration to use ORNa as an anode in SSBs. The crystal structure of NVP was verified by X-ray diffraction in Fig. S14 (online). The area loading of NVP in the cathode is about 3−4 mg cm^{-2}, and 5 μL of carbonate-based electrolyte is adopted to wet the cathodic side. The rate capability of ORNa/NZSP/NVP cell is examined by cycling at increasing current densities, as shown in Fig. 6a, demonstrating that the cell maintains high capacities of 111.1, 110.3, 107.9, and 103.0 mAh g^{-1} at the rates of 0.2, 0.5, 1 and 2 C, respectively. With the increase of current density, the polarization only exhibits a slight increase (Fig. 6b). Moreover, the ORNa/NVP full cell shows excellent cycling performance at 0.5 C (Fig. 6c), with a capacity of 110 mAh g^{-1} upon the first cycle discharge and a capacity of 106.9 mAh g^{-1} after 500 cycles with a high retention ratio of 95.4%. The performance of Na/NZSP/NVP cell with pristine Na metal anode is also evaluated under the same conditions. The impedance spectrum of quasi-solid-state batteries with standing time is consistent with previous observations of symmetric cells (Fig. S15 online), further confirming the inhibition of ORNa on unfavorable interfacial reactions. For the Na/NVP full cell, rapid capacity fading occurred after 20 cycles at 0.5 C (Fig. 6c), indicating the unstable cycling performance. The voltage shows inferior and asymmetric curves with increasing polarization (Fig. S16 online), probably due to the overpotential caused by the contact loss at the Na-NZSP interface (as shown in Fig. S17 online). The superior performance of the ORNa/NVP quasi-solid-state battery demonstrates the high cycling stability of the ORNa-NZSP interface, showing the great potential of the ORNa anode in solid-state battery applications.

4. Conclusion

In this work, we studied the interface chemistry between pristine Na and NZSP and illustrated the degradation mechanism caused by the original SEI. First-principle

calculations suggest that introducing oxygen into the sodium metal can affect the electron distribution around the sodium atom and reduce the chemical activity of sodium. A small amount of oxygen is introduced into the sodium metal by thermal treatment, to successfully generate a homogenous SEI between sodium and NZSP. The interface resistance between ORNa and NZSP is reduced to 0 Ω cm^{-2} and remains stable for 5 months, indicating its kinetic stability and no additional ion transport resistance. Benefiting from the oxygen-regulated spontaneous SEI, the symmetric cell shows a high average CCD of 6.3 mA cm^{-2} (60 °C) and a stable galvanostatic cycling for more than 6600 h at 0.5 mA cm^{-2} and 3 mAh cm^{-2} (RT). The full cell of ORNa/NVP is demonstrated to render an excellent rate performance and a high reversible capacity of 110 mAh g^{-1} with a capacity retention of 95.4% after 500 cycles under 0.5 C at room temperature. Such oxygen-regulated spontaneous SEI provides a more homogeneous plating/stripping process that inhibits the formation of interfacial voids, and thus significantly stabilizes the anode-SE interface. This oxygen-regulated spontaneous passivation SEI strategy may provide an avenue for achieving high stability at the anode-SE interface in solid-state alkali metal batteries.

Conflicts of interest

The authors declare that they have no conflict of interest.

Acknowledgements

This work was supported by the National Key R&D Program (2022YFB2502000), Zhejiang Provincial Natural Science Foundation of China (LZ23B030003), and the Fundamental Research Funds for the Central Universities (2021FZZX001-09).

Author contributions

Yinzhu Jiang conceived this idea and directed this project. Keshuang Cao performed the experiments and contributed to data interpretation. Yufan Xia performed the first-principle calculations. Haosheng Li helped in the assembly of quasi-solid-state cells

and XPS analysis. Huiqin Huang helped in preparing the solid electrolyte. Sikandar Iqbal, Muhammad Yousaf and Ben Bin Xu discussed the results and commented on the manuscript. Yinzhu Jiang, Hongge Pan, and Mi Yan supervised the project. All the authors approved the final version of the manuscript.

References

[1] Lou S, Zhang F, Fu C, et al. Interface issues and challenges in all-solid-state batteries: Lithium, sodium, and beyond. Adv Mater 2021; 33: 2000721.

[2] Ni Q, Xiong Y, Sun Z, et al. Rechargeable sodium solid-state battery enabled by in situ formed Na-K interphase. Adv Energy Mater 2023; 13: 2300271.

[3] Tang B, Yu X, Gao Y, et al. Positioning solid-state sodium batteries in future transportation and energy storage. Sci Bull 2022; 67: 2149-2153.

[4] Li Y, Li M, Sun Z, et al. Recent advance on NASICON electrolyte in solid-state sodium metal batteries. Energy Storage Mater 2023; 56: 582-599.

[5] Monroe C, Newman J. The impact of elastic deformation on deposition kinetics at lithium/polymer interfaces. J Electrochem Soc 2005; 152: A396.

[6] Cheng EJ, Sharafi A, Sakamoto J. Intergranular Li metal propagation through polycrystalline $Li_{6.25}Al_{0.25}La_3Zr_2O_{12}$ ceramic electrolyte. Electrochim Acta 2017; 223: 85-91.

[7] Chen R, Li Q, Yu X, et al. Approaching practically accessible solid-state batteries: Stability issues related to solid electrolytes and interfaces. Chem Rev 2019; 120: 6820-6877.

[8] Gao Z, Yang J, Li G, et al. TiO_2 as second phase in $Na_3Zr_2Si_2PO_{12}$ to suppress dendrite growth in sodium metal solid-state batteries. Adv Energy Mater 2022; 12: 2103607.

[9] Kim S, Yoon G, Jung S-K, et al. High-power hybrid solid-state lithium-metal batteries enabled by preferred directional lithium growth mechanism. ACS Energy Lett 2022; 8: 9-20.

[10] Cao K, Ma Q, Tietz F, et al. A robust, highly reversible, mixed conducting sodium metal anode. Sci Bull 2021; 66: 179-186.

[11] Miao R, Wang C, Li D, et al. Uniform Na metal plating/stripping design for highly reversible solid-state Na metal batteries at room temperature. Small 2022; 18: 2204487.

[12] Wang X, Chen J, Mao Z, et al. In situ construction of a stable interface induced by the SnS_2 ultra-thin layer for dendrite restriction in a solid-state sodium metal battery. J Mater Chem A 2021; 9: 16039-16045.

[13] Yang J, Gao Z, Ferber T, et al. Guided-formation of a favorable interface for stabilizing Na metal solid-state batteries. J Mater Chem A 2020; 8: 7828-7835.

[14] Xiang L, Jiang D, Gao Y, et al. Self-formed fluorinated interphase with Fe valence gradient for dendrite-free solid-state sodium-metal batteries. Adv Funct Mater 2023; 2301670.

[15] Wang Y, Wang Z, Zheng F, et al. Ferroelectric engineered electrode-composite polymer electrolyte interfaces for all-solid-state sodium metal battery. Adv Sci 2022; 9: 2105849.

[16] Wang T, Duan J, Zhang B, et al. A self-regulated gradient interphase for dendrite-free solid-state Li batteries. Energy Environ Sci 2022; 15: 1325-1333.

[17] Goodenough JB, Kim Y. Challenges for rechargeable Li batteries. Chem Mater 2010; 22: 587-603

[18] Banerjee A, Wang X, Fang C, et al. Interfaces and interphases in all-solid-state batteries with inorganic solid electrolytes. Chem Rev 2020; 120: 6878-6933.

[19] Seh ZW, Sun J, Sun Y, et al. A highly reversible room-temperature sodium metal anode. ACS Cent Sci 2015; 1: 449-455.

[20] Wang L, Ren N, Yao Y, et al. Designing solid electrolyte interfaces towards homogeneous Na deposition: Theoretical guidelines for electrolyte additives and superior high-rate cycling stability. Angew Chem Int Ed 2023; 62: e202214372.

[21] Zheng X, Fu H, Hu C, et al. Toward a stable sodium metal anode in carbonate electrolyte: A compact,

inorganic alloy interface. J Phys Chem Lett 2019; 10: 707-714.
[22] Zhou L, Cao Z, Zhang J, et al. Engineering sodium-ion solvation structure to stabilize sodium anodes: Universal strategy for fast-charging and safer sodium-ion batteries. Nano Lett 2020; 20: 3247-3254
[23] Tian Z, Zou Y, Liu G, et al. Electrolyte solvation structure design for sodium ion batteries. Adv Sci 2022; 9: 2201207
[24] Li Q, Cao Z, Cheng H, et al. Electrolyte boosting microdumbbell-structured alloy/metal oxide anode for fast-charging sodium-ion batteries. ACS Mater Lett 2022; 4: 2469-2479
[25] Lazar M, Kmiec S, Joyce A, et al. Investigations into reactions between sodium metal and $Na_3PS_{4-x}O_x$ solid-state electrolytes: Enhanced stability of the Na_3PS_3O solid-state electrolyte. ACS Appl Energy Mater 2020; 3: 11559-11569.
[26] Chi X, Zhang Y, Hao F, et al. An electrochemically stable homogeneous glassy electrolyte formed at room temperature for all-solid-state sodium batteries. Nat Commun 2022; 13: 2854.
[27] Deng T, Ji X, Zou L, et al. Interfacial-engineering-enabled practical low-temperature sodium metal battery. Nat Nanotechnol 2021; 17: 269-277.
[28] Wan TH, Saccoccio M, Chen C, et al. Influence of the discretization methods on the distribution of relaxation times deconvolution: Implementing radial basis functions with DRTtools. Electrochim Acta 2015; 184: 483-499.
[29] Kresse G, Furthmüller J. Efficient iterative schemes for ab initio total-energy calculations using a plane-wave basis set. Phys Rev B 1996; 54: 11169-11186.
[30] Kresse G, Furthmüller J. Efficiency of ab-initio total energy calculations for metals and semiconductors using a plane-wave basis set. Comput Mater Sci 1996; 6: 15-50.
[31] Blöchl PE. Projector augmented-wave method. Phys Rev B 1994; 50: 17953-17979.
[32] Perdew JP, Burke K, Ernzerhof M. Generalized gradient approximation made simple. Phys Rev Lett 1996; 77: 3865-3868.
[33] Tran R, Xu Z, Radhakrishnan B, et al. Surface energies of elemental crystals. Sci Data 2016; 3: 160080.
[34] Wang J, Wang S-Q. Surface energy and work function of fcc and bcc crystals: Density functional study. Surf Sci 2014; 630: 216-224.
[35] Grimme S, Antony J, Ehrlich S, et al. A consistent and accurate ab initio parametrization of density functional dispersion correction (DFT-D) for the 94 elements H-Pu. J Chem Phys 2010; 132: 154104.
[36] Wang V, Xu N, Liu J-C, et al. VASPKIT: A user-friendly interface facilitating high-throughput computing and analysis using VASP code. Comput Phys Commun 2021; 267: 108033.
[37] Momma K, Izumi F. VESTA3 for three-dimensional visualization of crystal, volumetric and morphology data. J Appl Crystallogr 2011; 44: 1272-1276.
[38] Zhang Z, Wenzel S, Zhu Y, et al. $Na_3Zr_2Si_2PO_{12}$: A stable Na^+-ion solid electrolyte for solid-state batteries. ACS Appl Energy Mater 2020; 3: 7427-7437.
[39] Wang S, Xu H, Li W, et al. Interfacial chemistry in solid-state batteries: Formation of interphase and its consequences. J Am Chem Soc 2018; 140: 250-257.
[40] Giordani V, Walker W, Bryantsev VS, et al. Synergistic effect of oxygen and $LiNO_3$ on the interfacial stability of lithium metal in a Li/O_2 battery. J Electrochem Soc 2013; 160: A1544.
[41] Haas R, Janek J. The influence of oxygen dissolved in the liquid electrolyte on lithium metal anodes. J Electrochem Soc 2022; 169: 110527.
[42] Lu K, Xu H, He H, et al. Modulating reactivity and stability of metallic lithium via atomic doping.

J Mater Chem A 2020; 8: 10363-10369.
[43] Gibson JS, Narayanan S, Swallow JEN, et al. Gently does it!: *In situ* preparation of alkali metal–solid electrolyte interfaces for photoelectron spectroscopy. Faraday Discuss 2022; 236: 267-287.
[44] Eichelberger RL. The solubility of oxygen in liquid sodium: A recommended expression. California: Atomics International; 1968.
[45] Meddeb S, Courouau J-L, Rouhard M, et al. Effect of temperature and dissolved oxygen content on the dissolved iron concentration in liquid sodium at equilibrium. J Nucl Mater 2022; 566: 153785.
[46] Adams PF, Hubberstey P, Pulham RJ. Review of the solubility of non-metals in liquid lithium. J Less-Common Met 1975; 42: 1-11.
[47] Oh JAS, Sun J, Goh M, et al. A robust solid-solid interface using sodium-tin alloy modified metallic sodium anode paving way for all-solid-state battery. Adv Energy Mater 2021; 11: 2101228.
[48] Ortmann T, Burkhardt S, Eckhardt JK, et al. Kinetics and pore formation of the sodium metal anode on NASICON-type $Na_{3.4}Zr_2Si_{2.4}P_{0.6}O_{12}$ for sodium solid-state batteries. Adv Energy Mater 2022; 13: 2202712.
[49] Zhu Y, He X, Mo Y. Origin of outstanding stability in the lithium solid electrolyte materials: insights from thermodynamic analyses based on first-principles calculations. ACS Appl Mater Interfaces 2015; 7: 23685-23693.
[50] Koshikawa H, Matsuda S, Kamiya K, et al. Dynamic changes in charge-transfer resistance at Li metal/$Li_7La_3Zr_2O_{12}$ interfaces during electrochemical Li dissolution/deposition cycles. J Power Sources 2018; 376: 147-151.
[51] Lu Y, Zhao C-Z, Huang J-Q, et al. The timescale identification decoupling complicated kinetic processes in lithium batteries. Joule 2022; 6: 1172-1198.

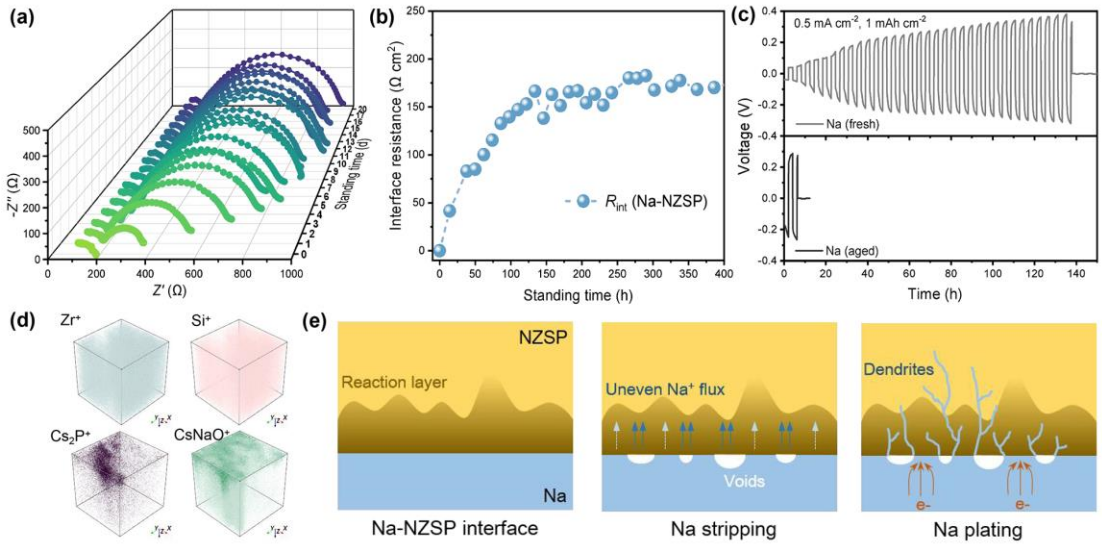

Fig. 1. (Color online) Investigation of the interface between pristine Na and NZSP. (a) Time-resolved impedance spectroscopy of the Na symmetric cell during 20 d. (b) R_{int} evolution of the Na symmetric cell. (c) Galvanostatic cycling profiles of the fresh Na and aged Na symmetric cells under the current density of 0.5 mA cm^{-2}. (d) 3D view of Zr^+, Si^+, Cs_2P^+, and $CsNaO^+$ distributions in the TOF-SIMS sputtered volumes of NZSP after contacting with Na, a, the analysis area is (100 × 100) μm^2. (e) Schematic illustrations of the degradation mechanism in Na-NZSP interface.

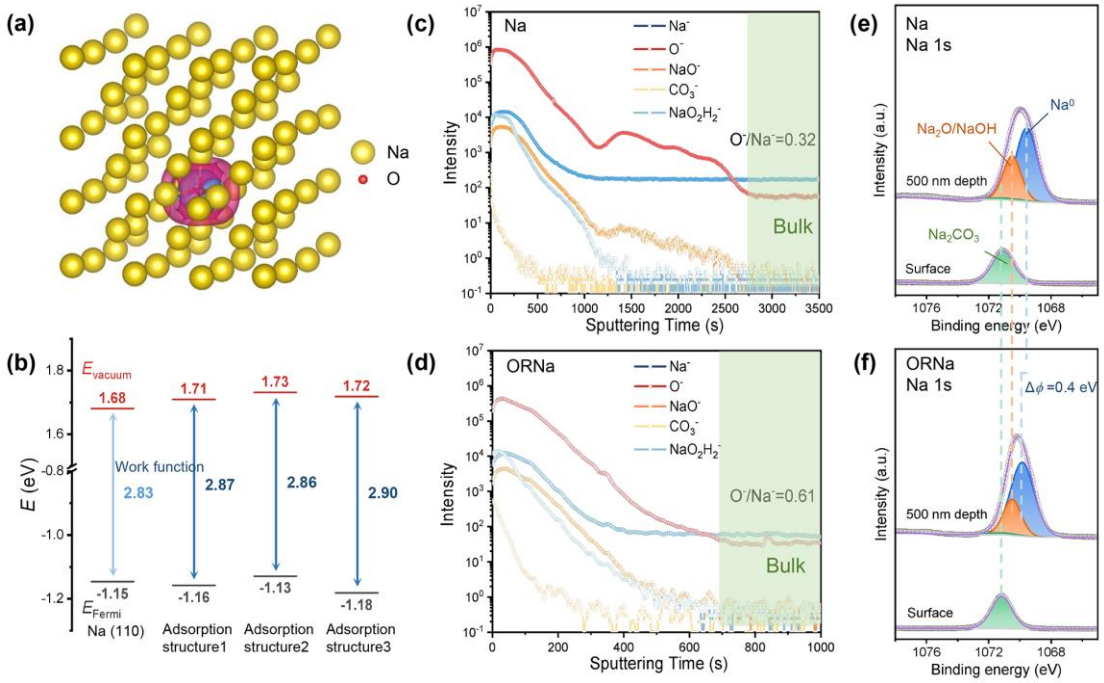

Fig. 2. (Color online) Theoretical calculations and characterization of ORNa. (a) Charge density difference of bulk sodium metal with an interstitial oxygen defect, the navy blue and crimson isosurfaces represent the increase and decrease in electron density, respectively (isovalue = 1.5×10^{-3} e Bohr^{-3}). (b) The calculated Fermi energy level (E_{Fermi}), vacuum energy level (E_{vacuum}) and corresponding work function of Na (110) surface and Na (110) + O_2 surfaces. TOF-SIMS depth profiles of pristine Na (c) and ORNa (d). High-resolution XPS spectra of Na 1s collected on the pristine Na € and ORNa (f) surfaces.

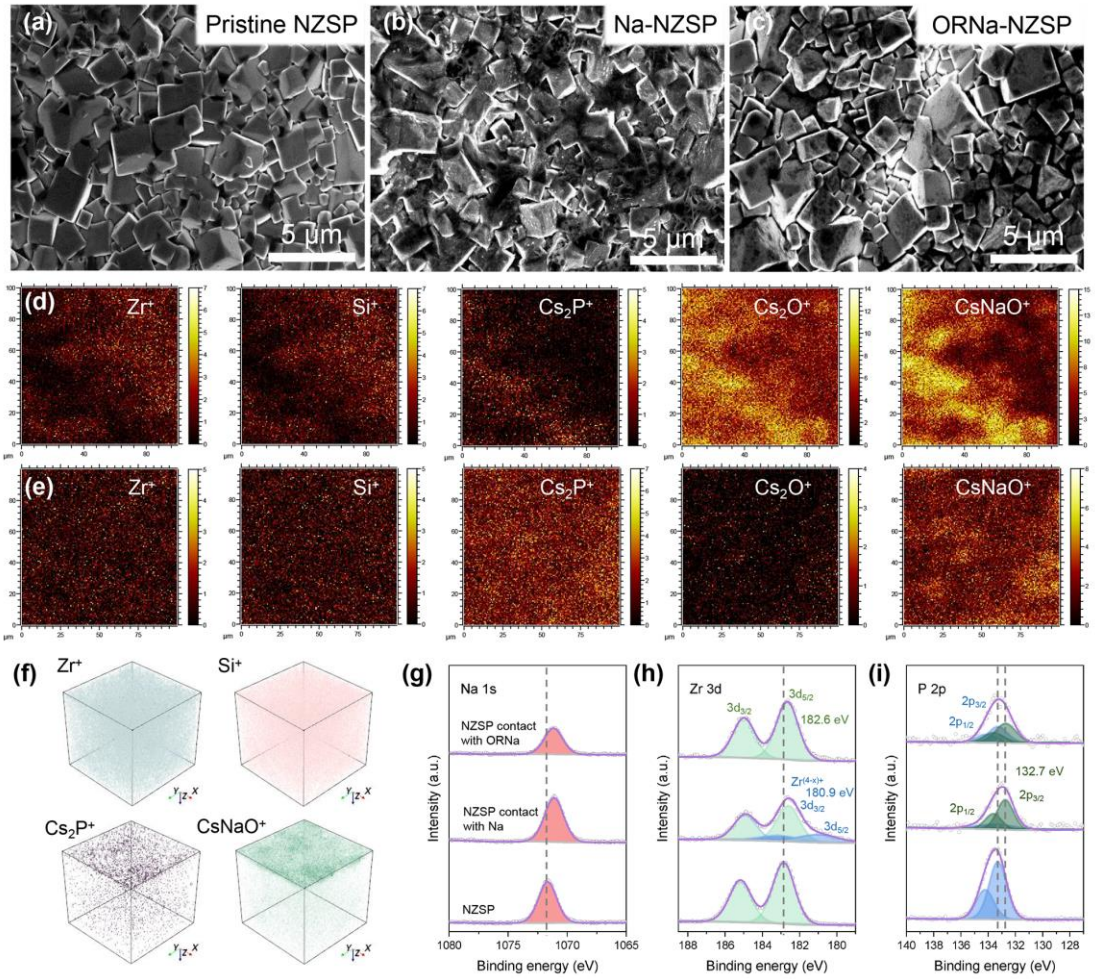

Fig. 3. (Color online) Interface chemistry between ORNa and NZSP. Top SEM views of the pristine NZSP (a), NZSP after contact with Na (b), and NZSP after contact with ORNa (c). TOF-SIMS mapping of NZSP after contact with Na (d) and ORNa (e). (f) 3D view of Zr^+, Si^+, Cs_2P^+, and $CsNaO^+$ distributions in the TOF-SIMS sputtered volumes of NZSP after contacting with ORNa. (g) Na 1s, (h) Zr 3d, and (i) P 2p XPS survey spectra of NZSP before and after contact with Na and ORNa.

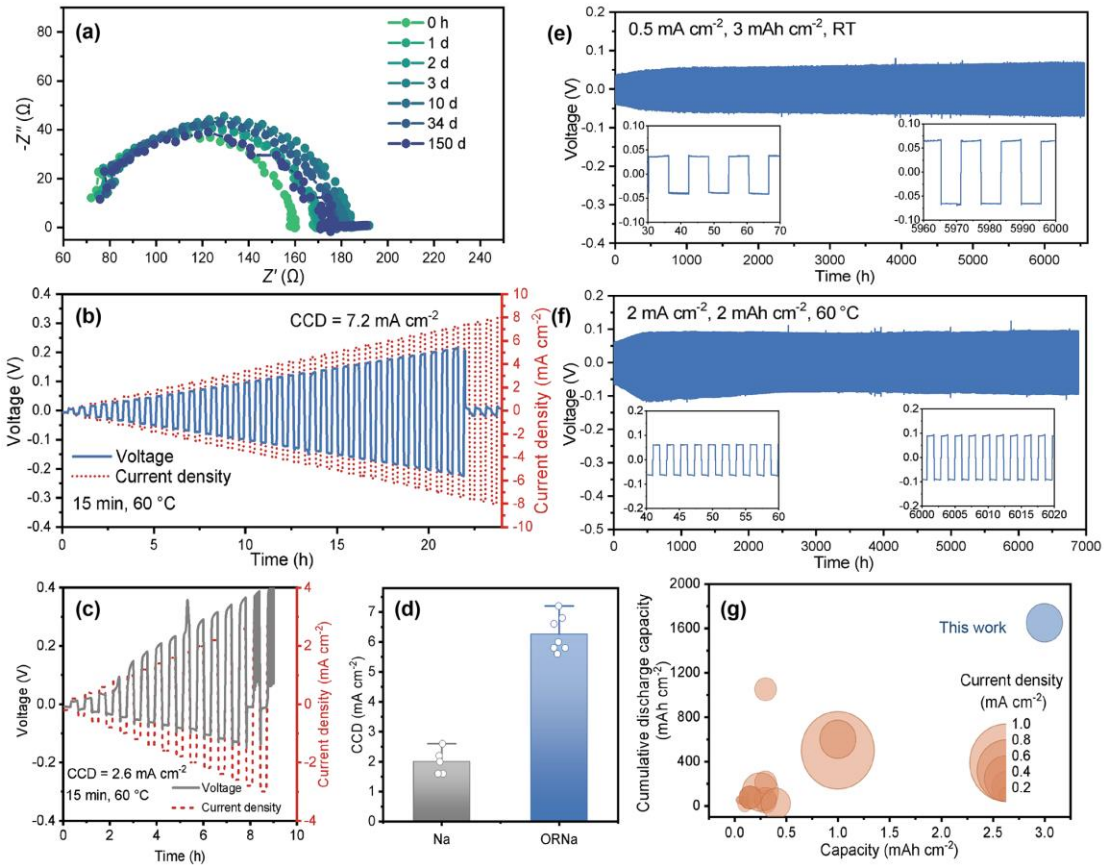

Fig. 4. (Color online) Electrochemical performance of ORNa. (a) Time-resolved impedance spectroscopy of the ORNa symmetric cell during 150 d. CCD measurement on the ORNa (b) and Na (c) symmetric cell at 60 °C. (d) Statistics of CCD data for the Na and ORNa symmetric cells. Dots represent the collected values of different cells. (e) Galvanostatic cycling profile of ORNa symmetric cell at 0.5 mA cm^{-2}, 3 mAh cm^{-2} (per half cycle), and RT. (f) Galvanostatic cycling profile of ORNa symmetric cell at 60 °C. (g) Comparison of cycling performance of this work and recently reported optimized symmetric cell based on NZSP at room temperature. The corresponding table is listed in Table S1 (online).

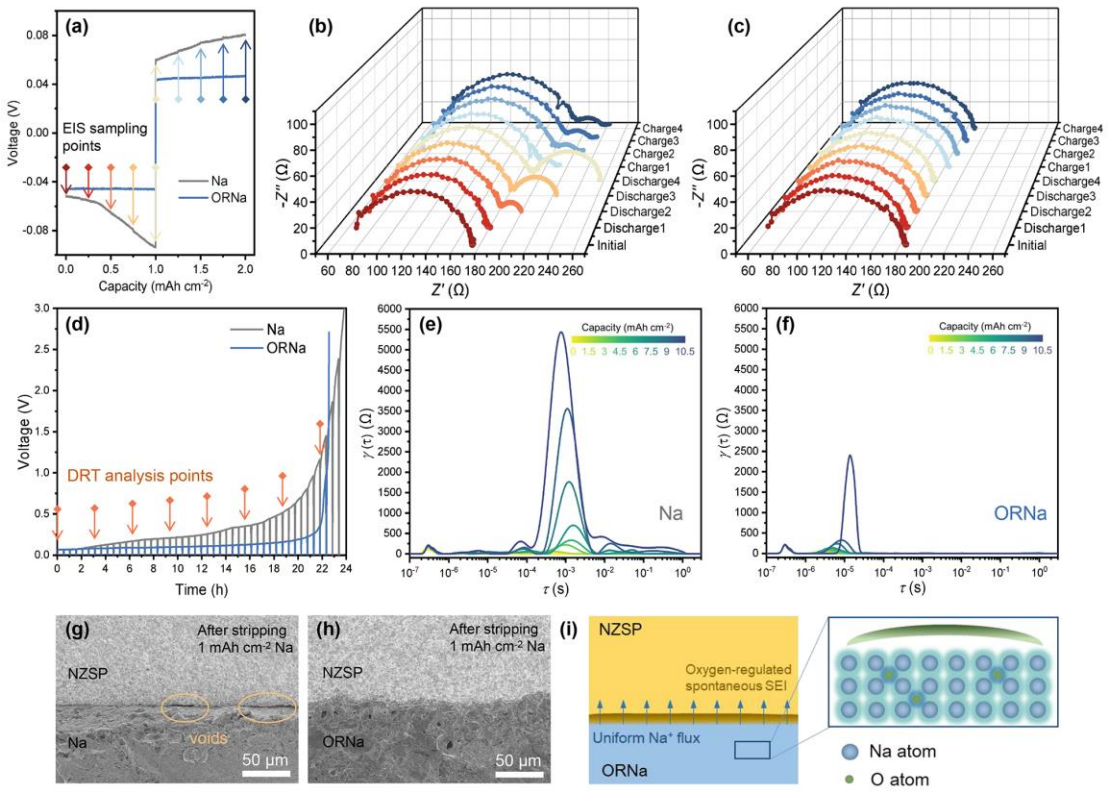

Fig. 5. (Color online) Investigation of the stability mechanism of ORNa-NZSP interface. (a) Voltage curves of Na and ORNa symmetric cells during charging and discharging at 0.5 mA cm^{-2}. EIS of Na (b) and ORNa (c) symmetric cells at different stages of charge and discharge. (d) Voltage profile of Na and ORNa symmetric cells in which one electrode was anodically dissolved at a current density of 0.5 mA cm^{-2} under RT. DRT calculated from EIS measurements at different states of charge in Fig. 5d, where I is Na symmetric cell and (f) is ORNa symmetric cell. Typical cross-section SEM images of Na/SE interface (g) and ORNa/SE interface (h) after stripping 1 mAh cm^{-2} at 0.5 mA cm^{-2}, the initial morphology of the interfaces are shown in Fig. S13 (online). (i) Schematic diagram of stability mechanism in ORNa-NZSP interface.

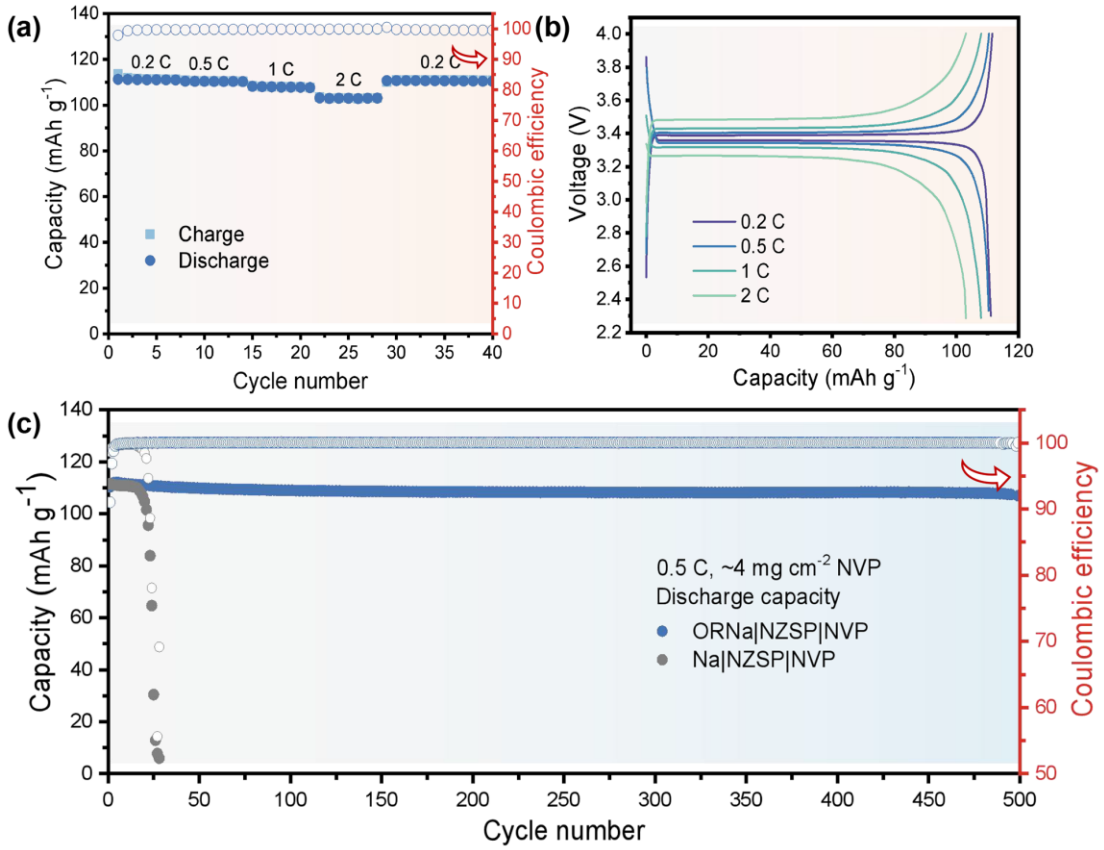

Fig. 6. (Color online) Electrochemical performance of quasi-solid-state batteries. Rate performances (a) and charge/discharge curves (b) for the ORNa/NZSP/NVP full cells. (c) The galvanostatic cycling performance of the Na/NZSP/NVP and ORNa/NZSP/NVP full cells under a current rate of 0.5 C at room temperature.